

FULL PAPER

Open Access



Quantitative strong motion simulations at three locations in downtown Mashiki during the 2016 Kumamoto Earthquake (Mw 7.0) based on the nonlinear ground response analyses with soil liquefaction

Kiyoshi Fukutake^{1*}, Kazuhiro Yoshida¹, Hiroshi Kawase², Fumiaki Nagashima² and Jikai Sun²

Abstract

The mainshock of the 2016 Kumamoto Earthquake (Mw 7.0) caused extensive damage to buildings in downtown Mashiki, Kumamoto Prefecture, Japan. The heavy building damage in the area was associated with both strong ground motion and building response characteristics. Fortunately, there were two strong motion stations in the area and the observed records during the mainshock were distributed, showing peak ground velocities exceeding 100 cm/s on the surface. The level of shaking would be sufficient to make soft surface sediments nonlinear. To reproduce observed ground motions quantitatively, one-dimensional nonlinear effective-stress time-history analyses were conducted at three locations in downtown Mashiki. The input wave was employed as either the observed underground wave or simulated outcrop input motion based on the diffuse field theory. The main purpose of the study was twofold: to investigate the proper soil constitutive relationship and its nonlinear parameters based on the limited amount of in situ information, and to validate the method of input motion evaluation at the seismological bedrock level based on diffuse field theory. The nonlinear time history analyses using the on-site boring survey and the outcrop wave based on diffuse field theory showed that the waveform of the mainshock observed on the ground surface was explained with sufficient accuracy. In addition, the results of the effective stress analysis indicated that soil liquefaction might have occurred in the area with thick surface layers along the Akitsu River where the water table was considered to be quite shallow.

Keywords Kumamoto earthquake, Observed strong motion, Nonlinear analysis, On-site boring survey, Soil liquefaction, Diffuse field theory

*Correspondence:

Kiyoshi Fukutake
kiyoshi.fukutake@shimz.co.jp

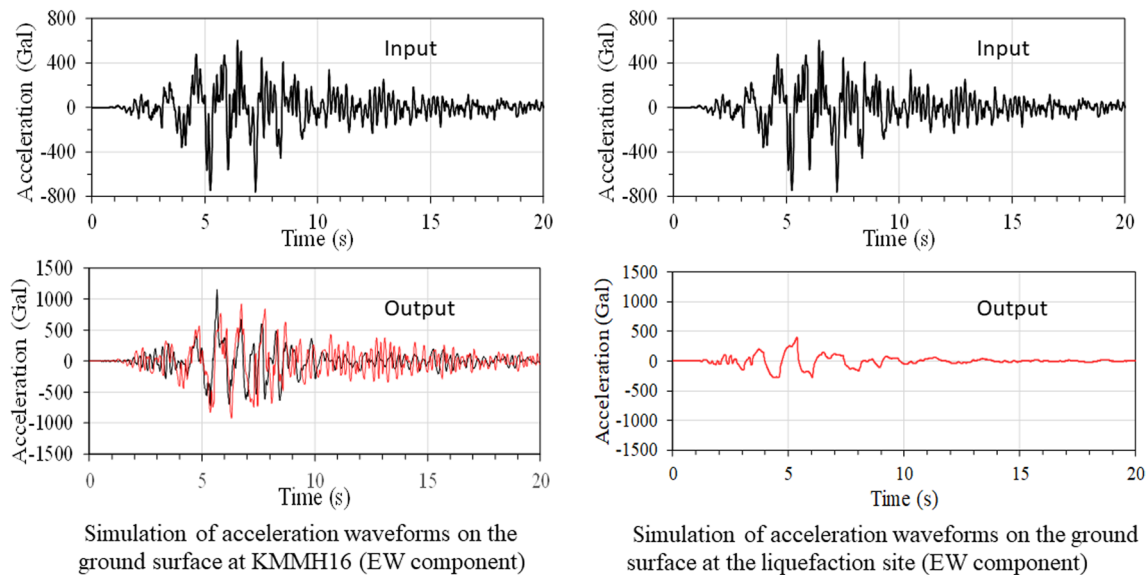
Full list of author information is available at the end of the article



© The Author(s) 2023. **Open Access** This article is licensed under a Creative Commons Attribution 4.0 International License, which permits use, sharing, adaptation, distribution and reproduction in any medium or format, as long as you give appropriate credit to the original author(s) and the source, provide a link to the Creative Commons licence, and indicate if changes were made. The images or other third party material in this article are included in the article's Creative Commons licence, unless indicated otherwise in a credit line to the material. If material is not included in the article's Creative Commons licence and your intended use is not permitted by statutory regulation or exceeds the permitted use, you will need to obtain permission directly from the copyright holder. To view a copy of this licence, visit <http://creativecommons.org/licenses/by/4.0/>.

Graphical Abstract

Quantitative Strong Motion Simulations at Three Locations in Downtown Mashiki during the 2016 Kumamoto Earthquake (Mw 7.0) Based on the Nonlinear Ground Response Analyses with Soil Liquefaction



Introduction

During the 2016 Kumamoto Earthquake of Mw 7.0 (Japan Meteorological Agency's magnitude M_{JMA} 7.3), a VII intensity in the seismic intensity scale of Japan Meteorological Agency (JMA) was recorded in downtown Mashiki, which is located near the western segment of the Futagawa fault. Figure 1 shows the distribution of the damage ratios of buildings (mainly wooden houses) located in downtown Mashiki (NILM: National Institute for Land and Infrastructure Management 2016; Kashiwa et al. 2019). A similar distribution and actual damage within this damage concentration area were also reported by Kawase et al. (2017). The damage survey shown in Fig. 1 was conducted by a reconnaissance team examining the apparent structural damage from outside based on the definition created by Okada and Takai (1999) of heavy damage or collapse. The damage was small along the Akitsu River; however, it increased farther into the northern area.

Strong earthquake records were obtained from the ground surface and in the borehole at the KiK-net observation station (KMMH16) in the northeastern corner of the target area (Fig. 1). At the Mashiki Town Office (MTO), earthquake motions were also recorded on the first (ground) floor of the building. These two sites were the only sites with mainshock records in the target area.

Under these circumstances, Nakagawa et al. (2017) have simulated the observation wave obtained on the ground surface using equivalent linear analysis. In addition, Kashiwa et al. (2019) and Nakano et al. (2018) have performed nonlinear time history analysis, but no comparison with surface acceleration records has been shown in their papers. Because clear evidence of liquefaction along the Akitsu River has been reported (National Research Institute for Earth Science and Disaster Resilience 2016; Wakamatsu et al. 2017), effective stress analysis for soil liquefaction is required. Therefore, a boring survey was conducted at the GS-MSK-2 site (Shingaki et al. 2017), around which sand boils caused by liquefaction were observed.

Here, to establish a proper approach for quantitative reproduction of ground motions based on nonlinear ground response analyses (nGRA) during the 2016 Kumamoto Earthquake, nonlinear time history analyses (both the total stress analysis and effective stress analysis considering excess pore water pressure) were conducted at the three locations (KMMH16, MTO, and GS-MSK-2) depicted in Fig. 1. This is a necessary step to explain the cause of the damage distribution in downtown Mashiki, as shown in Fig. 1. Regarding the damage simulation in Mashiki, this has previously been reported elsewhere based on the velocity structures in the area

by microtremors and the damage prediction model of wooden houses in Japan (Sun et al. 2020, 2021). However, the details of the validation exercise of the nGRA approach, especially on the proper choice of the constitutive relationship, material damping, and input ground motions used, were established and reported in this study.

Regarding the nonlinear behavior of soil layers near the surface, a novel equivalent-linear ground response analysis (eLGRA) based on the effective shear strain inside a thin slice of soil layers was first proposed by Idriss and Seed (1968) and then extended by Schnabel et al. (1972) as a distributed code called SHAKE. Since then, eLGRA has been used extensively to investigate the nonlinear behavior of soil sediments during strong shaking (see reviews in Finn 1988; Finn 1991; Beresnev and Wen 1996), primarily because eLGRA only requires the shear modulus degradation (G/G_0) curve and increasing damping curve with respect to the effective shear strain. However, eLGRA is a total-stress analysis and cannot represent the effects of the pore water pressure built up inside the water-saturated soil during strong shaking. In addition, the accuracy of the eLGRA simulation decreased as the maximum shear strain exceeded a certain threshold ($\sim 0.1\%$), which depends on the soil type as well as the definition of the desired accuracy.

Realistic numerical simulations of nonlinear ground responses based on the effective stress analysis (esGRA) have been reported in the 1990s after extensive model developments on nonlinear constitutive relationships and liquefaction characteristics in the early 1970s (see reviews in Iwasaki 1986; Youd 2003; Idriss and Boulanger 2008; National Academy of Science 2016). It is noteworthy that the borehole array observation in the Wildlife Liquefaction Array observed strong motion records with liquefaction during strong shaking of the M6.5 Superstition Hills earthquake of 1987 (Holzer et al. 1989; Prevost et al. 1991; Hushmand et al., 1992; Zeghal and Elgamal 1994; Holzer and Youd 2007). Since then, strong ground motions have been observed at sites with clear evidence of liquefaction during the 1989 Loma Prieta earthquake (Finn et al. 1993; Boulanger et al. 1998), the 1994 M6.9 Northridge earthquake (Holzer et al. 1999; Pretell et al. 2020), the 1995 M6.9 Kobe earthquake (Kawase et al. 1995, 1996; Elgamal et al. 1996), the 2011 M6.1 Canterbury (Christchurch) earthquake (Wotherspoon et al. 2014), and the 2011 M9.0 Off the Pacific Coast of Tohoku, Japan earthquake (Fukutake and Jang 2013). Although significant efforts have been devoted to reproduce the observed surface ground motions with the effects of excess pore water pressure, including liquefaction, the level of reproducibility depends on-site conditions and

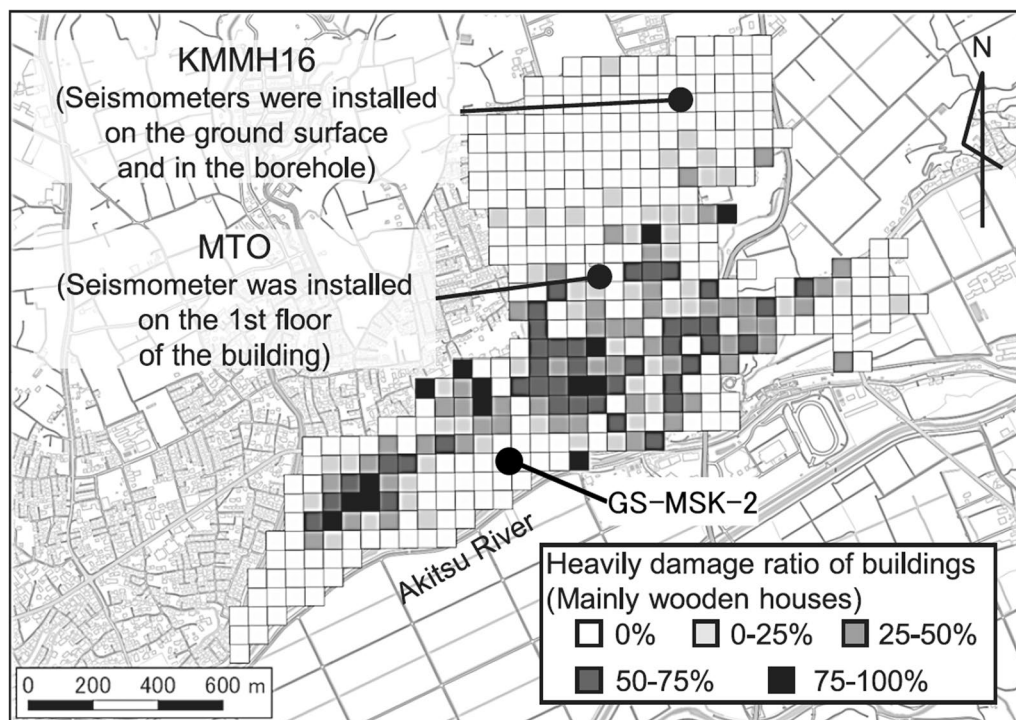


Fig. 1 Distribution of heavily damaged ratios of residential houses in Mashiki town by NILIM (2016), with the locations of the three analysis sites (Kashiwa et al. 2019)

availability of the constraints on the soil parameters used in the numerical simulation, the correction of which could be very costly. Therefore, it is essential to perform a parametric study for numerical simulation analysis to validate the current methodology for quantitative simulation of observed strong motions considering the effect of accumulated pore water pressure inside saturated soil.

As mentioned earlier, it was fortunate that there was a vertical array strong motion station, KMMH16, and the KiK-net Mashiki station. At KMMH16, acceleration records have been obtained in the vertical array, one on the ground surface, and the other at 252 m below the ground surface (Aoi et al. 2000; NIED 2022b). A nonlinear time history analysis (total stress analysis) at KMMH16 was conducted in this study using the observed borehole record first and then an outcrop input motion estimated by using the diffuse field concept on the observed records at KMMH16. At the MTO site, the groundwater level was used as a parameter for effective stress analysis. GS-MSK-2 is a boring site near the Akitsu River (Shingaki et al. 2017) and is in the area where sand boiling due to soil liquefaction has been confirmed (NIED 2022a; Wakamatsu et al. 2017), and the damage to buildings was minor (Fig. 1). At this site, effective stress analysis considering the liquefaction of sand layers was conducted to examine the degree of liquefaction. At these two sites, it was assumed that the same outcrop input as at KMMH16 impinged on the bottom of the seismological bedrock, and then the input motions on the engineering bedrock were calculated based on the linear ground response analysis for the layers between the seismological bedrock and engineering bedrock. In the following analyses, scattering damping was employed as Rayleigh-type damping, the value of which was determined based on parametric studies. The use of one-dimensional modeling in this study can be justified because gently inclined layer interfaces were found from north to south with an inclination of tens of meters in 2 km based on the velocity profile inversions for the entire area of downtown Mashiki (Sun et al. 2020).

The soil constitutive equations used in this study are the modified Ramberg–Osgood model (R–O model, Tatsuoka and Fukushima 1978) and the modified General Hyperbolic Equation model (GHE model, Tatsuoka and Shibuya 1992; Murono 1999) for the shear stress–shear strain relationship. The Bowl model (Fukutake and Jang 2013; Fukutake and Kiriyaama 2018; Fukutake 2018) is employed for the shear strain–dilatancy relationship in effective stress analysis for liquefaction. The effectiveness of the Bowl model used in this study was verified by simulation analyses of vertical array records for the 1987 Superstition Earthquake (Fukutake et al. 1992) and the 1995 Kobe earthquake (Kawase et al. 1995, 1996). The

esGRA code used here is termed HiPER (Fukutake and Kiriyaama 2018), in which soil nonlinearity is extended into three-dimensional space (in two horizontal components and one vertical component) for the stress–strain relationship. Parameters of the stress–strain model are determined from dynamic deformation tests ($G/G_0 \sim \gamma$ and $h \sim \gamma$ relationships, where γ is the shear strain), whereas parameters of the Bowl model are determined from the liquefaction resistance tests (laboratory element test) in principle. In the following analyses, the focus is on the EW component because it is the major-axis component.

Simulation using KMMH16 borehole records

The first target was the KiK-net observation station in Mashiki, KMMH16, a nationwide network of strong-motion seismographs installed by the National Research Institute for Earth Science and Disaster Resilience, Japan (NIED). KMMH16 is located in the northeastern part of downtown Mashiki in Kumamoto Prefecture and has strong motion records of the 2016 Kumamoto Earthquake sequence on the ground surface and in the borehole. On the ground surface, the recorded maximum acceleration and velocity were more than 1000 Gal and 100 cm/s, respectively. Nakagawa et al. (2017) conducted laboratory tests to obtain dynamic deformation characteristics of soil samples and performed a simulation analysis of observation records of the Kumamoto Earthquake using equivalent linear analysis. In the present study, the dynamic deformation characteristics were approximated by two types of constitutive equations to compare their performances, and records were simulated using one-dimensional nonlinear time history analysis. The reason why small damage ratios were observed around KMMH16 despite its observed high maximum velocity is considered to be the construction age of the houses around KMMH16. They were relatively new, mostly built after 1981, when significant building code modifications were implemented (e.g., Yamada et al. 2017; Sun et al. 2021).

Table 1 shows the ground soil profile at KMMH16. The shear wave velocities (V_s) of each layer down to the borehole depth have been determined by compressional and shear wave (P-S) logging, as shown on NIED's website (NIED 2022b). The shallow part of the ground was characterized by four soft layers (No. 1–4) on a hard layer (No. 5, rock) with V_s of 500 m/s. The natural period of the eigenvalue analysis when the bottom of the model was fixed was 0.91 s for the primary mode and 0.41 s for the secondary mode. The unit volume weight γ_t of soil was estimated using the following equation (Kobayashi et al. 1995):

Table 1 Ground profiles of KMMH16 (KiK-net Mashiki) by the boring data from NIED website

No.	GL m	Layer thickness m	Soil profile		γ_t kN/m ³	V_s m/s
1	3.0	3.0	Non-linear, K-1	Volcanic clay	15.9	110
2	9.0	6.0	Non-linear, K-2	Volcanic clay	16.9	240
3	14.0	5.0	Non-linear, K-3	Sand	16.9	240
4	15.0	1.0	Non-linear, K-3	Sand	16.9	240
5	33.0	18.0	Linear	Pumice tuff	18.4	500
6	41.0	8.0	Non-linear	Volcanic clay	17.9	400
7	51.0	10.0	Non-linear	Sand	19.4	760
8	69.0	18.0	Non-linear	Sandy gravel	19.4	760
9	101.0	32.0	Linear	Tuff breccia	19.7	820
10	133.0	32.0	Linear	Andesite rock	21.7	1470
11	143.0	10.0	Linear	Tuff breccia	19.2	700
12	167.0	24.0	Linear	Andesite rock	21.4	1380
13	200.4	33.4	Linear	Tuff	19.7	840
14	234.0	33.6	Linear	Andesite rock	21.7	1470
15	252.0	18.0	Linear	Andesite rock	24.5	2700

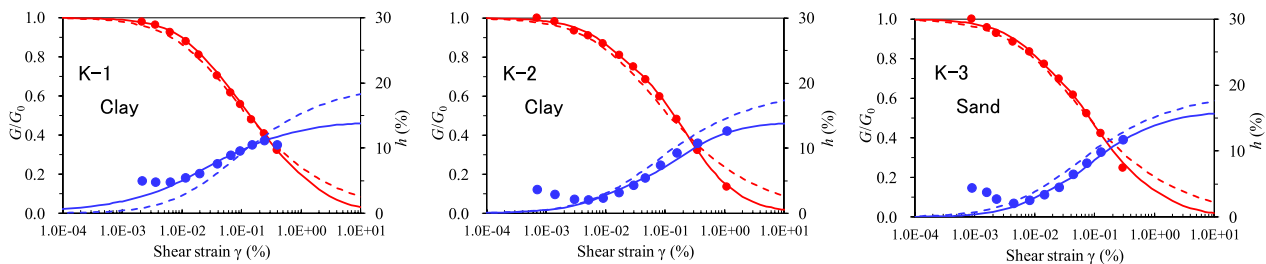


Fig. 2 $G/G_0 \sim \gamma$, $h \sim \gamma$ relations of soils at KMMH16 site and fitting of models. (filled red circle, filled blue circle: experimental results, broken lines: R–O model, solid lines: GHE model)

$$\gamma_t = 9.8 \left(1.4 + 0.67 \sqrt{V_s} \right), \quad V_s : \text{km/s.} \quad (1)$$

Nonlinear characteristics of layers No. 1–4 have been investigated by Nakagawa et al. (2017) using laboratory dynamic deformation tests. For the nonlinearity of layers No. 6–8, the test results of Nakagawa et al. (2017) have been applied mutatis mutandis. The other rock layers were assumed to be linear. The bottom of the analysis model (GL-252 m) was assumed to be a rigid boundary where the observed acceleration motion in the borehole was applied as a “within-layer” motion at this stage of analysis.

Two types of soil constitutive equations have been employed in this study: the R–O model (Tatsuoka and Fukushima 1978) and the GHE model (GHE model, Tatsuoka and Shibuya 1992; Murono 1999). Both are hysteresis function type models using the Masing rule; the R–O model is an exponential type constitutive equation with three parameters, while the GHE model is a hyperbolic type constitutive equation with ten parameters (see Appendix). Although there is a sand layer below the water table, it is clear from the acceleration waveforms that there was no liquefaction at this site; therefore, an effective-stress analysis was not performed.

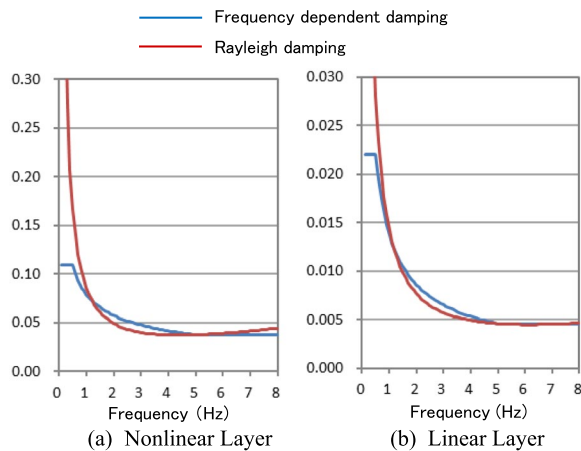


Fig. 3 Comparison of frequency-dependent damping and Rayleigh damping

Figure 2 compares the results of the dynamic deformation test at KMMH16 performed by Nakagawa et al. (2017) with the fitting results using the two types of constitutive equations. The experimental values were characterized by a smaller hysteresis damping constant h than general cohesive and sandy soil, especially sandy soil. The GHE model showed better agreement with the experimental results over a wider range of strain levels, likely because the GHE model had more parameters than the R–O model.

The actual ground attenuation should include both hysteresis damping and scattering damping. Only the hysteresis damping is often considered in a typical nonlinear analysis, however, scattering damping is introduced to reproduce the waveform from the main wave with large strain levels to the coda part of the wave with smaller strain levels. In the present study, scattering damping is expressed using Rayleigh-type damping. Nakagawa et al. (2017) have introduced the frequency-dependent scattering damping $h = h_0 * f^\alpha$ as follows:

$$\text{Non-linear layers : } h_0 = 0.07924, \alpha = -0.46, \quad (2)$$

$$\text{Linear layers : } h_0 = 0.01377, \alpha = -0.68. \quad (3)$$

It should be noted that the values were assumed to be constant in the frequency range lower than 0.5 Hz or higher than 5 Hz. To set the parameters of Rayleigh-type damping, the frequency range was considered from 0.5 to 5.0 Hz, and was assumed to match the above frequency-dependent damping at 5.0 Hz. The two parameters of Rayleigh-type damping were determined to minimize the sum of the squares of the absolute values of the differences from the frequency-dependent damping, with frequency as the weighting factor. The values obtained are shown below:

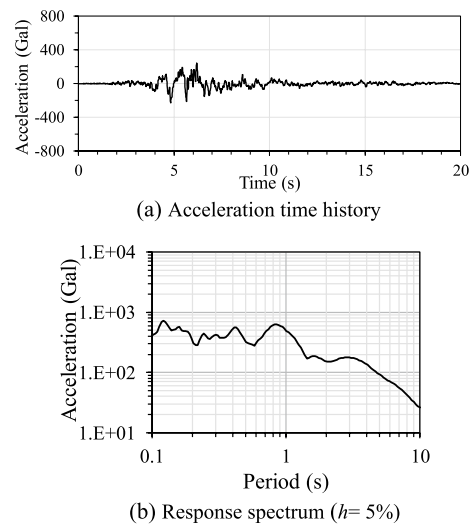


Fig. 4 Acceleration time history and Response spectrum of input wave at KMMH16 (GL-252 m, Observed record, EW component)

$$\text{Non - linear layers : } a_0 = 1.0315, \alpha_1 = 0.001361, \quad (4)$$

$$\text{Linear layers : } a_0 = 0.1748, \alpha_1 = 0.0001164, \quad (5)$$

where the damping matrix is constructed as a linear combination of mass and stiffness matrices as $[C] = \alpha_0[M] + \alpha_1[K]$.

Figure 3 shows a comparison between the frequency-dependent attenuation in Eqs. (2) and (3) and the obtained Rayleigh-type damping in Eqs. (4) and (5). Fukutake et al. (2020) have also reported that observation records may be simulated better using scattering damping in addition to hysteresis damping.

In Fig. 4, the acceleration waveforms of the input wave and its response spectrum 252 m below ground level are plotted. They were observed in the borehole during the main shock of the Kumamoto Earthquake.

Figure 5a shows a comparison between the acceleration waveforms of the observed record and the one-dimensional nonlinear time history analysis results using the two constitutive equations in the East–West (EW) direction on the ground surface. The phase was reproduced well in both constitutive equations. The maximum value at 5.6 s seemed to be slightly underestimated in the analyses, and this tendency was particularly remarkable in the GHE model. The acceleration waveform reaches a peak because the stress–strain relationship in the GHE model is a hyperbolic curve and rapidly reaches the upper limit. Figure 5b shows the acceleration response spectra of these simulated waves. The analysis results showed a significant increase near the fundamental resonance period of the ground, at 0.9 s. Figure 6 shows the depth distribution

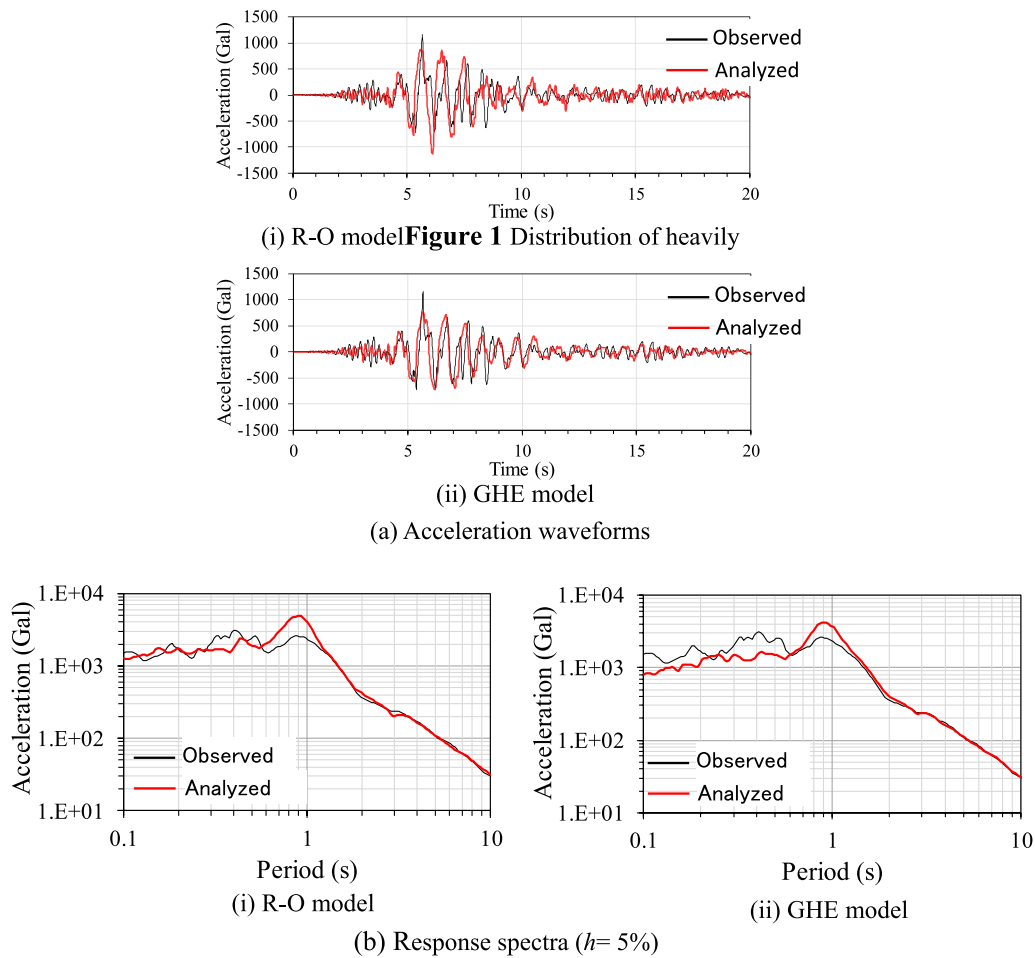


Fig. 5 Comparison of acceleration waveforms and response spectra on the ground surface at KMMH16 (EW component)

of the maximum acceleration of the simulated waveforms within each layer. In the R–O model, the correspondence of the peak ground acceleration (PGA) of the simulated accelerogram with the observed PGA was very good. If the waveform in Fig. 5a is closely examined, however, the maximum value of the calculated acceleration corresponds to the opposite phase of the observed acceleration.

Figure 7 shows the depth distribution of the maximum shear strain. Large values were observed in the sand layers (layers Nos. 3 and 4) with V_s of 240 m/s. In particular, the maximum value was found at the bottom of these layers. This corresponds to the maximal impedance contrast at the interface between the linear and nonlinear soil behavior in the simulation. The difference between the two models was remarkable in layers No. 1–4. Compared to that of the R–O model, the GHE model obtained larger strain in layers Nos. 3 and 4, while the strain in layers Nos. 1 and 2 was smaller. This seemed to be the so-called seismic isolation effect of sand layers Nos. 3 and 4. As a result, it might be inferred that the GHE model

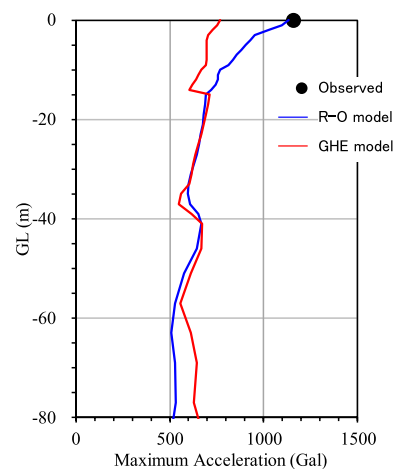


Fig. 6 Distribution of maximum acceleration at KMMH16 (EW component)

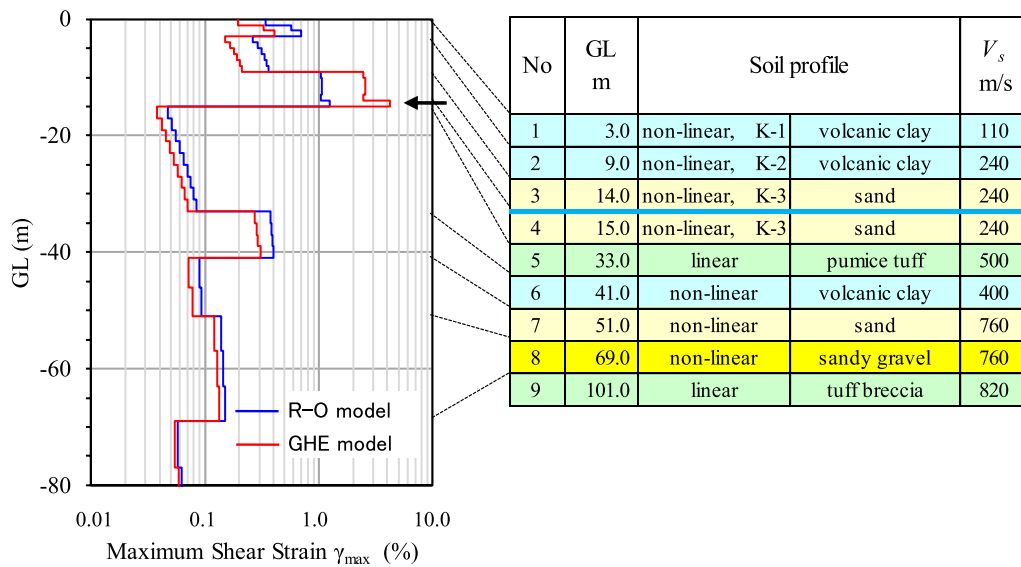


Fig. 7 Distribution of maximum shear strain at KMMH16

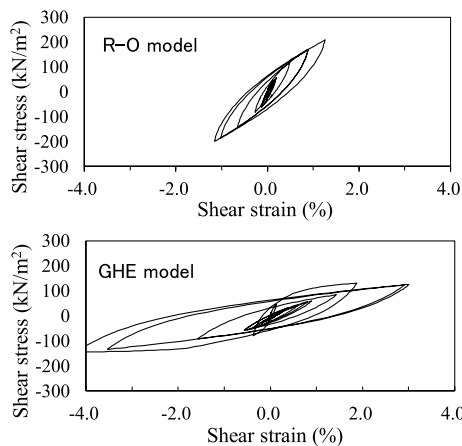


Fig. 8 Shear stress–shear strain relationship at KMMH16 (GL-14 m ~ -15 m, sand layer No. 4 shown in Fig. 3)

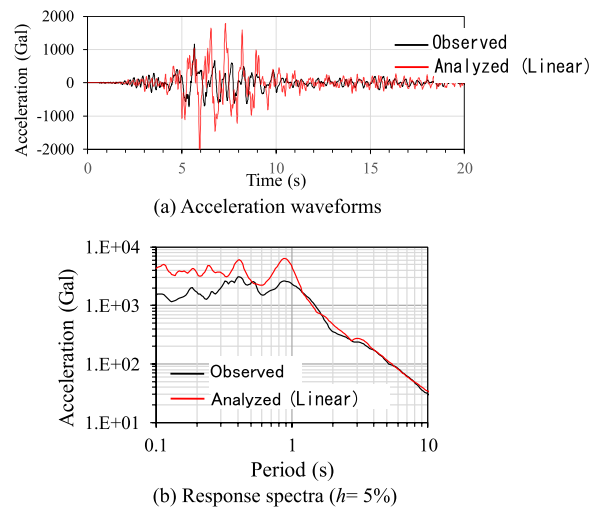


Fig. 9 Comparison of acceleration waveforms and response spectra on the ground surface at KMMH16 (linear case, EW component)

underestimated the observed acceleration on the ground surface.

The shear stress–shear strain relationship of sand layer No. 4 (the reference point is indicated in Fig. 7) is shown in Fig. 8. In the R–O model, the maximum shear strain was approximately 1.2%, whereas it was 4% in the GHE model. Since the GHE model was a hyperbolic model in terms of the shear stress–strain relationship, the shear stress reached the upper limit when it reached the fracture line and the shear strain after that became quite large. This may be a primary cause of the underestimation of the PGA in the GHE model shown in Fig. 5a.

Based on these results, it was decided to use the R–O model in the following analyses, which was more

reproducible as a whole. Using the GHE model at the points where excess pore water pressure occurred (MTO, GS-MSK-2) was also tried, but the acceleration amplitude was too small to reproduce the acceleration waveform well.

A linear analysis was also performed to confirm the effects of nonlinearity of the ground at KMMH16. Rayleigh damping was set the same as in the nonlinear case. Figure 9 shows the acceleration waveforms and acceleration response spectra obtained by the linear analysis in comparison to the observed record, respectively. From these figures, it was confirmed that the amplitude was overestimated and the pulse appearance time (phase)

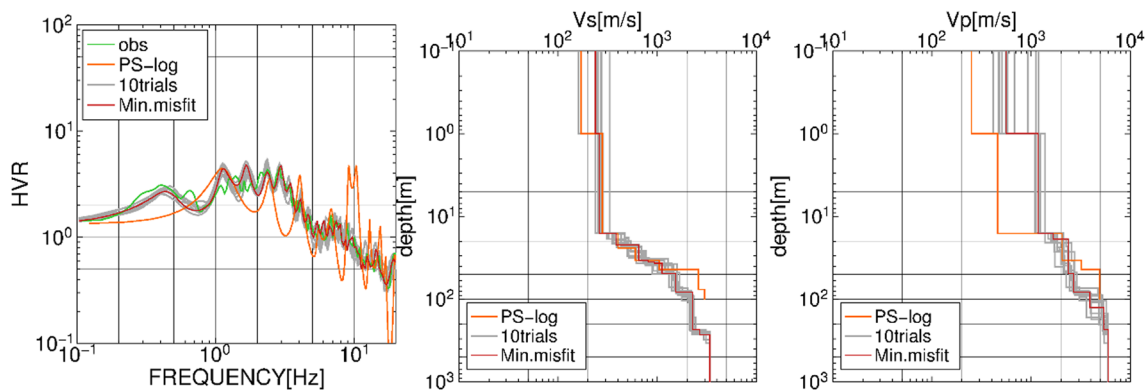


Fig. 10 Identification results by diffuse field theory at KMMH16

was earlier in the linear analysis than those in the observation. Thus, from this evidence, the shallow part of the ground at KMMH16 went into the nonlinear regime during the mainshock of the 2016 Kumamoto Earthquake.

Estimation of the incident wave based on diffuse field theory

In the previous section, the observed borehole record at KMMH16 was used as the input wave for the analysis model. However, it is difficult to reproduce the response on the ground surface at an arbitrary site other than KMMH16 with this borehole record because reflected waves from the surface and the layer interfaces would not be the same at other sites with different profiles. Therefore, in this section, the diffuse field theory of earthquake motion (Kawase et al. 2011) is employed to estimate the horizontal incident wave on the seismic bedrock from the vertical motion observed on the ground surface.

Based on the diffuse field theory, the earthquake horizontal-to-vertical spectral ratio (EHVR) is the ratio of the horizontal and vertical amplification factors between the seismic bedrock and the ground surface ($|TF_{horizontal}|$ and $|TF_{vertical}|$) with a coefficient of the P-wave velocity (V_p) and V_s of the bedrock, α and β , as shown in Eq. (6):

$$\frac{H}{V} = \sqrt{\frac{\alpha}{\beta} \frac{|TF_{horizontal}|}{|TF_{vertical}|}}, \tag{6}$$

where H and V represent the Fourier spectral amplitudes of the horizontal and vertical components of the earthquake motion recorded on the ground surface, respectively. TF is the transfer function of the surface motion relative to the outcrop motion; therefore, the absolute value of TF ($|TF|$) represents the amplification factor. As derived by Nagashima et al. (2017) and Nagashima and Kawase (2022), Eq. (7) is obtained by deforming Eq. (6):

$$\frac{H}{|TF_{horizontal}|} = \sqrt{\frac{\alpha}{\beta}} \frac{V}{|TF_{vertical}|}. \tag{7}$$

The spectrum of the ground surface is divided by the amplification factor to obtain the outcrop spectrum at the bottom of the velocity structure, which is used to calculate $|TF|$. In this section, $|TF_{horizontal}|$ and $|TF_{vertical}|$ are calculated from the V_s and V_p structures above the seismic bedrock, respectively. As a result, the horizontal outcrop spectral amplitude at the seismic bedrock is proportional to the vertical one, according to Eq. (7).

Assuming the establishment of a diffuse field during a single realization of an earthquake, it is possible to apply Eq. (7) to a single motion record. However, during strong motion, the nonlinear behavior of the shallow subsurface profiles can affect the horizontal amplification factor, while the vertical amplification factor tends to remain linear. By assuming linearity of the vertical amplification factor ($|TF_{vertical}|$) during strong shaking, the horizontal spectral amplitude at the seismic bedrock can be obtained using a linear approach by applying Eq. (7).

As mentioned earlier, the horizontal site amplification factor is affected by the nonlinear behavior of the shallow subsurface profiles during strong shaking. However, due to the complexity of the nonlinear parameters, it can be challenging to estimate the horizontal amplification factor for strong motions ($|TF_{horizontal}^{SM}|$). To estimate $|TF_{horizontal}^{SM}|$ without considering nonlinear parameters, an equation for the horizontal site amplification factor can be derived by modifying Eq. (6):

$$|TF_{horizontal}^{SM}| = \sqrt{\frac{\beta}{\alpha}} \frac{H^{SM}}{V^{SM}} |TF_{vertical}|, \tag{8}$$

where H^{SM} and V^{SM} represent the Fourier spectral amplitudes of the horizontal and vertical components of a strong motion, respectively. By assuming linearity of the vertical amplification factor ($|TF_{vertical}|$) during strong

shaking, $|TF_{horizontal}^{SM}|$ can be estimated without considering nonlinear parameters, by using the linear calculation from the right hand term of Eq. (8) is obtained. To apply Eqs. (7) and (8), it is necessary to have knowledge of the theoretical linear amplification characteristics of the vertical motions ($|TF_{vertical}|$). To obtain $|TF_{vertical}|$, the ground velocity structure was identified using the averaged EHVR calculated from 14 earthquake records with $MJMA > 5.5$ and $PGA < 50$ Gal observed at KMMH16 from January 2002 to March 2016. The EHVR was calculated using the waveforms of 40 s after the onset of the S wave for 14 earthquake records. Based on the diffuse field theory, the V_s , V_p , and layer thickness of the velocity model that minimized the residuals of the observed and theoretical EHVRs were identified using the Hybrid Heuristic Search method (Nagashima et al. 2014). It was assumed that V_s and V_p increased with depth (i.e., no velocity inversion layer). The bedrock velocities α and β were assumed to be 6.0 km/s and 3.4 km/s, respectively. The inversion was performed ten times with the same parameters, but with different random number seeds for initialization. Figure 10 shows the identification results. The results indicate that the obtained velocity structures have little variability among ten trials, but reproduce the observed EHVR quite well. The resultant velocity profiles from the seismological bedrock to the surface with the least misfit, as determined by the inversion process, are listed in Table 2. In the inversion process, $|TF_{horizontal}|$ corresponding to the V_s structure was determined such that it reproduces the peaks of the observed EHVR, and $|TF_{vertical}|$ corresponding to the V_p structure was

Table 2 Ground profiles at KMMH16 from the seismological bedrock inverted from EHVR

No.	GL m	Layer thickness m	γt kN/m ³	V_s m/s	V_p m/s
1	3.00	3.00	16.27	154.87	296.56
2	15.00	12.00	16.95	249.36	760.00
3	20.29	5.29	17.54	337.07	1841.61
4	22.39	2.10	18.33	483.09	1918.07
5	38.19	15.80	18.82	598.03	1995.00
6	50.69	12.50	19.31	733.19	1995.09
7	75.99	25.30	19.60	790.10	2529.23
8	92.12	16.13	19.70	827.70	2558.47
9	137.04	44.92	20.29	990.51	2768.98
10	166.27	29.23	20.87	1172.19	4078.39
11	230.87	64.60	21.66	1468.35	4796.23
12	246.39	15.52	22.54	1790.20	4813.21
13	1152.17	905.78	22.74	1871.20	5776.98
14	4252.48	3100.31	25.58	3264.74	5786.36
15	-	-	25.87	3400.00	6000.00

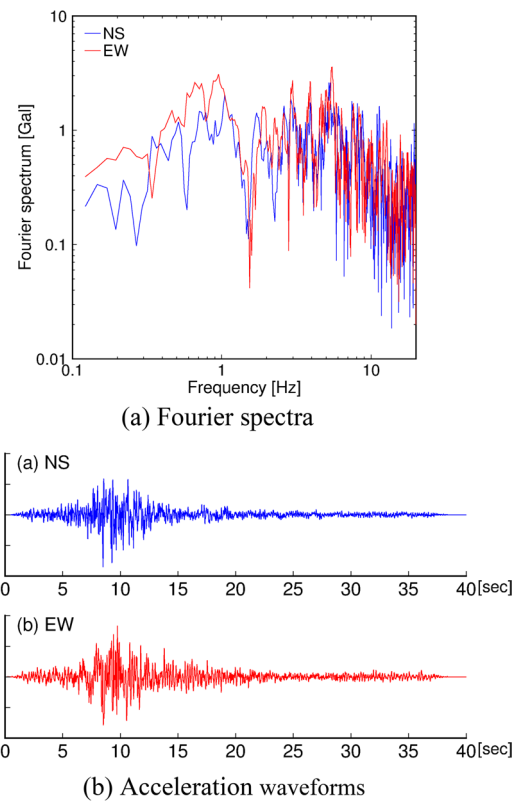


Fig. 11 Spectra and acceleration waveforms of input wave on seismic bedrock

calculated to reproduce the troughs of the observed EHVR. $|TF_{horizontal}|$ was constrained quite well by the observed EHVR as compared to $|TF_{vertical}|$, meanwhile, $|TF_{vertical}|$ was also sufficiently constrained by the observed EHVR with precision.

Next, the horizontal amplification characteristics have been estimated from the horizontal and vertical motions observed on the ground surface and the theoretical vertical amplification characteristics based on Eq. (8). The mainshock record of the 2016 Kumamoto Earthquake at KMMH16 contained many factors that disturb the diffuse field, such as the radiation characteristics of the source, as the site is located near the Futagawa fault. The EHVR calculated from the main S-wave part of the mainshock (4–37 s in Fig. 4) shows a distinct shape not only in the high-frequency range, which is known to be affected by the nonlinear behavior of the shallow ground structure during strong shaking, but also in the low-frequency range, which corresponds to the deep-ground structure and is not affected by the nonlinear behavior. As such, we believe that the assumption of the establishment of the diffuse field during the main S-wave part is not valid. To overcome this, we attempted to find a wave portion that exhibits the same degree of nonlinearity in

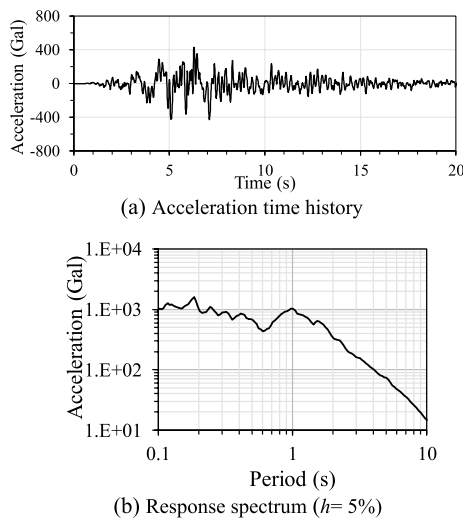


Fig. 12 Acceleration time history and response spectrum of input wave at KMMH16 (at GL-252 m, synthesized outcrop wave, EW component)

the high-frequency range as the main S-wave part and a similar shape of EHVR in the low-frequency range as the EHVR averaged from weak earthquake motions to assume the establishment of a diffuse field. Finally, we identified the latter half of the S wave and the coda part (9–37 s in Fig. 4). The obtained wave portion was used to predict the horizontal amplification characteristics ($|TF_{horizontal}^{SM}|$) during the mainshock based on Eq. (8). Dividing the spectrum of the entire waveform of the mainshock observed on the surface by the $|TF_{horizontal}|$ obtained in the previous step, as in the left-hand side of Eq. (7), the influence of the nonlinear site amplification was removed from the spectrum under the equivalent-linear assumption, and the incident wave on the seismic bedrock was estimated. Figure 11a shows the estimated Fourier spectra of incident waves on the seismic bedrock in the north–south (NS) and EW directions, and Fig. 11b shows the waveforms of the incident waves on the seismic bedrock calculated using the phase of the borehole records at KMMH16. The validity of these input horizontal motions on the seismic bedrock is confirmed through the eIGRA at KMMH16 (Sun et al. 2021).

In the following simulation analyses, the models were constructed considering the ground structure above the depth of the borehole survey. The obtained incident seismic waves on the seismic bedrock, as depicted in Fig. 11b, were transformed into outcrop waves at the bottom of the borehole survey using elastic calculations and the inverted velocity model shown in Fig. 10.

Simulation using the KMMH16 incident outcrop waves

The simulation analysis of the 2016 Kumamoto Earthquake mainshock at KMMH16 was performed again using soil profiles of P-S logging (Table 1) above the engineering bedrock using the incident outcrop waves obtained through the procedure in the previous section. While the simulated results using the borehole record as an input have been shown already, the analysis here is required because the validity of the simulated input at the bottom of the shallow soil layers above the engineering bedrock needs to be confirmed. In this case, an outcrop wave was used as the input motion in the considered model and was injected 252 m below the ground surface, assuming an elastic engineering bedrock. The R–O model was employed for the soil constitutive equation, as previously mentioned, based on a parametric study.

Figure 12 shows the acceleration waveform and acceleration response spectrum of the input wave (EW component) based on diffuse field theory, respectively. Comparisons of the calculated acceleration waveforms on the ground surface and their response spectra with the observed waveforms are shown in Fig. 13.

The phases were well matched to the main motions shown in Fig. 13a. In the trailing motions at approximately 10–15 s, the analysis results were slightly larger, probably because of a slightly larger amplitude of the input wave. The correspondence of the other parts of the acceleration motion and response spectra was sufficiently secured. From the above data, it was confirmed that the analysis results obtained using the input wave from the diffuse field theory in the previous section had the same degree of agreement as the results obtained when using the observed borehole records. Using this outcrop wave,

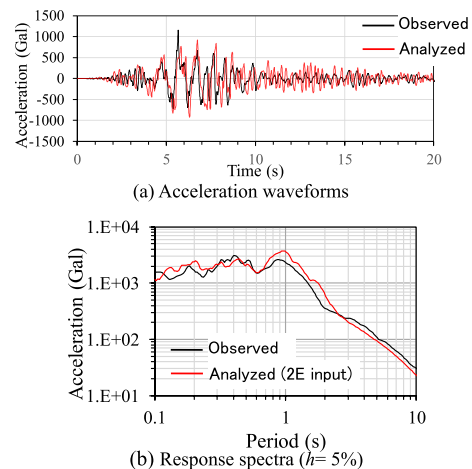


Fig. 13 Comparison of acceleration waveforms and response spectra on the ground surface at KMMH16 (EW component)

Table 3 Ground profiles of MTO (Mashiki Town Office) after Kashiwa et al. (2019)

No.	GL m	Layer thickness m	Soil profile		γ_t kN/m ³	V_s m/s	V_p m/s
1	4.95	4.95	M-1	Roam	15.7	140	
2	15.45	10.50	M-2	Sandy silt	15.7	190	
3	28.60	13.15	M-3	Sand	18.6	380	
4	47.45	18.85	M-3	Sand gravel	18.6	540	
5	50.00	2.55		Tuff (linear)	19.6	700	
					(damper)	19.6	700

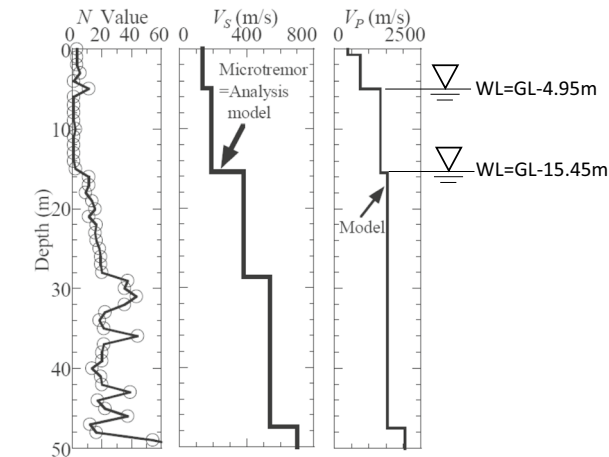


Fig. 14 SPT N-value, S-wave (V_s) and P-wave (V_p) velocity distribution at MTO (after Kashiwa et al. 2019)

strong-motion waveforms on the ground surface at points without borehole records were reproduced.

Nonlinear (effective stress) analysis at MTO

At the MTO observation point, the outcrop wave calculated using diffuse field theory as the outcrop of the

engineering bedrock was input into the bottom of the boring structure. Because it was unknown exactly what the groundwater level was at this site, the analysis was performed with the groundwater level as a parameter using the R-O model combined with the Bowl model, which can consider excess pore water pressure (Fukutake and Jang 2013; Fukutake and Kiriyaama 2018; Fukutake 2018). The MTO soil profiles obtained by Kashiwa et al. (2019) are presented in Table 3. The depth distribution of the standard penetration test, N -value, V_s , and V_p from Kashiwa et al. (2019) are shown in Fig. 14.

The groundwater level was analyzed in two patterns, GL-15.45 m and GL-4.95 m. GL-15.45 m is the groundwater level shown in Kashiwa et al. (2019). GL-4.95 m was set considering the V_p distribution in Kashiwa et al. (2019). This level has been determined because the V_p value suddenly increases at the GL-4.95 m stratum boundary, which is quite common as indirect evidence of the water saturation observed in the V_p profiles in Japan (Nagashima and Kawase 2021).

When the groundwater level was assumed to be GL-4.95 m, effective stress analysis was performed in the silt layer (No. 2) using the Bowl model to consider the excess pore water pressure (please note that

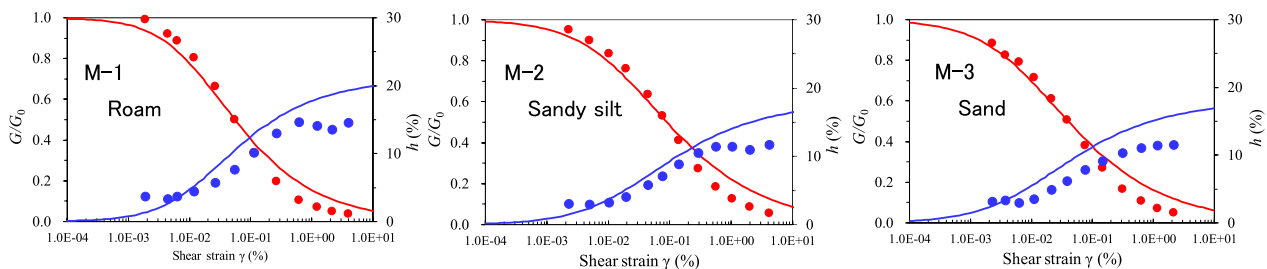


Fig. 15 $G/G_0 \sim \gamma$, $h \sim \gamma$ relations of soils at MTO and fitting of R-O model (filled red circle, filled blue circle: experimental results, solid lines: R-O model)

the results of the analysis did not lead to liquefaction in the end). For the Bowl model parameters, the standard parameter values listed in Fukutake (2018) were employed because no specific soil element test for water-saturated sand sampled in situ was conducted.

Figure 15 depicts the comparison between the results of the dynamic deformation test at the MTO performed by Kashiwa et al. (2019) and the fitting results using the R–O model. Because the $G/G_0-\gamma$ relationship was set to be more important, the damping constant h was allowed to be slightly larger than the experimental value.

Figure 16 shows the acceleration waveform and acceleration response spectrum of the input wave on the

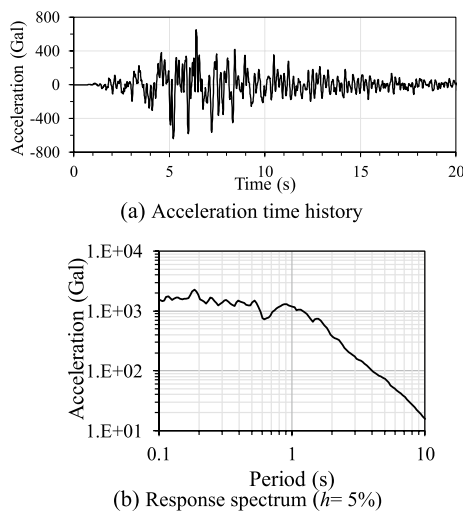


Fig. 16 Acceleration time history and response spectrum of input wave at MTO (at GL-50 m, synthesized outcrop wave, EW component)

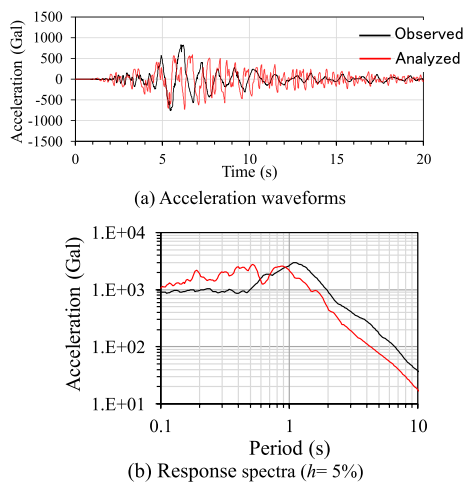


Fig. 17 Comparison of acceleration waveforms and response spectra at MTO (ground water level GL-15.45 m, EW component)

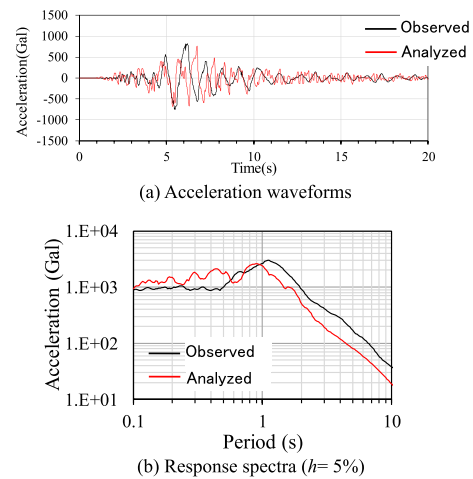


Fig. 18 Comparison of acceleration waveforms and response spectra on the ground surface at MTO (ground water level GL-4.95 m, EW component)

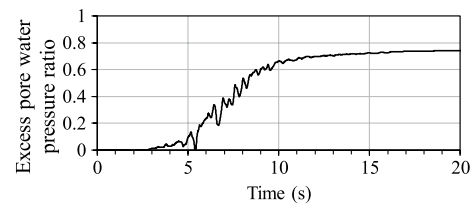


Fig. 19 Time history of excess pore water pressure ratio in sandy silt layer (GL-10 m)

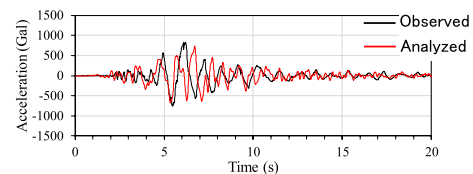


Fig. 20 Comparison of acceleration waveforms at MTO considering SSI effects (ground water level GL-4.95 m, EW component)

engineering bedrock at the MTO obtained using the diffuse field theory mentioned in the previous section.

Figure 17 shows comparisons are acceleration waveforms on the ground surface and response spectra when the groundwater level was assumed to be GL-15.45 m. Comparisons are also shown in Fig. 18 when the groundwater level was assumed to be GL-4.95 m. The amplitude is more suitable when the groundwater level is set to GL-4.95 m because the excess pore water pressure ratio increases by approximately 75% in the silt layer when the groundwater level is set to GL-4.95 m, as shown in Fig. 19. Because the silt layer softens as the water pressure increases, the amplitude of the subsequent motions

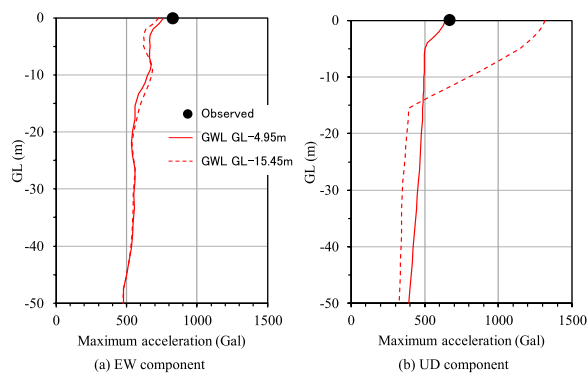


Fig. 21 Distribution of maximum acceleration at MTO

is suppressed. Focusing on the acceleration waveform, the analysis results had richer short-period components than those of the observed record. This is because the acceleration observation waveform shown in Fig. 18a was recorded on the first floor of a three-storied reinforced-concrete building; therefore, it should include the influence of soil–structure interaction effects, as discussed in Nakano et al. (2018). Here, the short-period components were simply reduced using Yamahara’s method (1970), which considers the soil–structural interaction effects by taking a moving average on the time axis. In this study, the time history was created using the moving average of 11 data points, 0.11 s in a duration. This is roughly equivalent to filtering at 10 Hz or higher; the results are shown in Fig. 20. The short-period components were suppressed, and compatibility with the observed record was improved.

Figure 21a shows the depth distribution of the maximum horizontal acceleration at MTO. The difference in the horizontal peak acceleration distribution owing to the difference in the groundwater level was small. The depth distribution of the maximum vertical acceleration is shown in Fig. 21b. When the groundwater level was set to GL-4.95 m, the estimated value of the vertical acceleration was in good agreement with the observed value, however, when the groundwater level was set to GL-15.45 m, the vertical acceleration was amplified in the shallower parts above the groundwater level, especially on the ground surface. This was because the bulk modulus of water was taken into consideration below the groundwater level, so the rigidity was high against the vertical strain; however, above the groundwater level, only the bulk modulus of the soil skeleton worked, and the rigidity was soft against the vertical strain. The effect of the P-wave velocity constant at the groundwater level is shown in Fig. 21b.

From the above results, it was inferred that the groundwater level at the time of the MTO should be approximately GL-5 m.

Nonlinear (effective stress) analysis at the GS-MSK-2 site

The sand boiling phenomenon due to liquefaction was observed near the GS-MSK-2 site during the 2016 Kumamoto Earthquake (NIED 2022a, 2022b). To confirm the simulation capability of the liquefaction analysis, the Bowl model was employed in combination with the R–O model, and an effective stress analysis was performed to consider the excess pore water pressure. A simulation analysis was performed using the outcrop wave obtained using diffuse field theory as the input to the boring structure closest to this point. The soil profiles are listed in Table 4 (Kurita et al. 2020). The groundwater level is assumed to be at the ground surface. The layers considering excess pore water pressure were layers 1–7. Layers No. 4 to No. 7 (GL-9 m to -18 m) of tuffaceous sand were considered liquefiable layers. Figure 22 shows the dynamic deformation test results at GS-MSK-2 (Shingaki et al. 2017) and the fitting results obtained using the R–O model. Because the G/G_0 - γ relationship was set to match the experimental values at the time of fitting, the damping constant h was allowed to be slightly larger than the experimental values, as was the case for MTO. Figure 23 shows the liquefaction strength curve for tuffaceous sand simulated by element tests using the R–O and Bowl models. The liquefaction strength curves were calculated using the standard values shown in Fukutake (2018) for the parameters of the Bowl model.

Figure 24 shows the acceleration input waveform and acceleration response spectrum based on diffuse field theory at the GS-MSK-2 site.

Figure 25 shows the acceleration waveform and acceleration response spectrum, respectively, on the ground surface. The acceleration amplitude became smaller owing to liquefaction from approximately 7 s, and the waveform included rich long-period components. Figure 26 shows the depth distribution of the excess pore water-pressure ratio. At the top of the tuffaceous sand layer, the excess pore water pressure ratio was 1.0, which led to liquefaction. Water pressure was also generated in the clay layer; however, liquefaction did not occur. Figure 27a shows the building-up process of the excess pore water pressure ratio of the tuffaceous sand layer (GL-10 m). It was 1.0 at 7 s, indicating the occurrence of liquefaction. Figure 27b shows the stress–strain relationship of the tuffaceous sand layer (GL-10 m). The maximum strain was nearly 5%, and the hard spring type stress–strain phenomenon was observed owing to the cyclic mobility. There were smaller damage ratios to wooden houses around this observation point (Fig. 1). This may be because the liquefaction of the ground suppressed the acceleration of the ground surface to some extent owing to the seismic

Table 4 Ground profiles of GS-MSK-2 after Kurita et al. (2020)

No.	GL m	Layer thickness m	Soil profile		γ_t kN/m ³	V_s m/s
1	2.0	2.0		Fill	15.3	90
2	7.0	5.0	T4-C1	Tuffaceous clay	15.4	80
3	9.0	2.0		Tuffaceous clay	15.4	120
4	11.0	2.0	T4-S1	Tuffaceous sand	16.8	160
5	12.0	1.0		Tuffaceous sand	16.8	210
6	15.0	3.0		Tuffaceous sand	16.8	250
7	18.0	3.0		Tuffaceous sand	16.8	290
8	22.0	4.0	T4-S2	Tuffaceous sand	16.8	330
9	28.0	6.0	T4-S3	Tuffaceous sand	16.8	360
10	35.0	7.0	T4-S4	Tuffaceous sand	16.8	440
11	48.0	13.0	T4-G1	Tuffaceous gravel	17.0	520
12	53.0	5.0		Tuffaceous silty sand	16.8	400
13	60.0	7.0		Tuffaceous gravel	17.0	500
14	68.0	8.0		Tuffaceous gravel	17.0	700
15	75.0	7.0		Tuff (linear)	18.0	800
(damper)					18.0	800

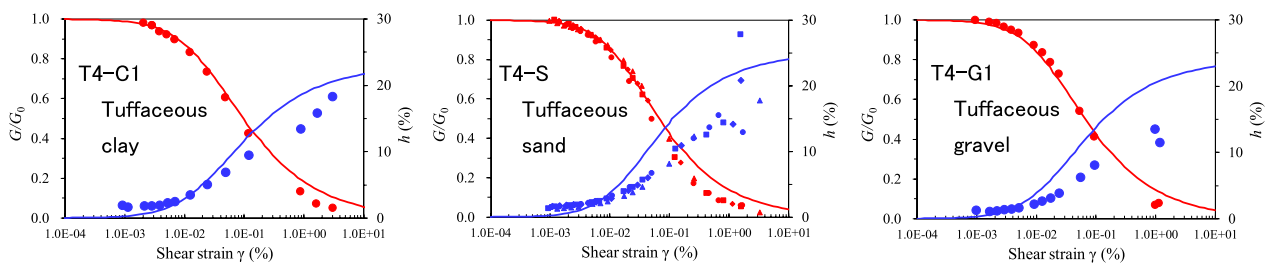


Fig. 22 $G/G_0 \sim \gamma$, $h \sim \gamma$ relations of soils at GS-MSK-2 and fitting of R-O model (symbols: experimental results, solid lines: R-O model)

isolation effects. As described above, it was theoretically confirmed that liquefaction layers were formed in a region with a thick soft surface layer and a shallower water table along the Akitsu River. This conclusion matches the local survey results shown in NILM (2016) and NIED (2022b).

Concluding remarks

In this study, a nonlinear time history simulation was performed at three observation locations in Mashiki town during the 2016 Kumamoto Earthquake based on boring data and estimated input motions at the bottom of the boring layers. The input motion corresponds to the outcrop motion and is fed at the base of the soil column,

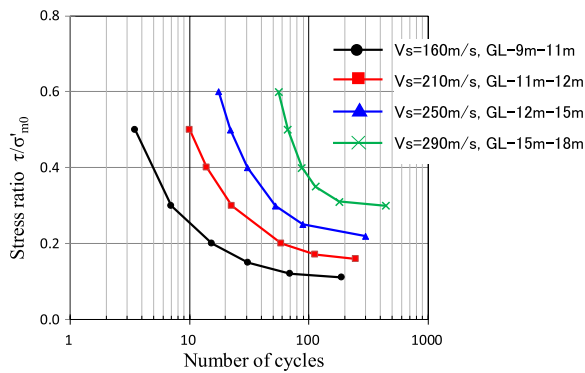


Fig. 23 Liquefaction resistance curves in tuffaceous sand layer at GS-MSK-2

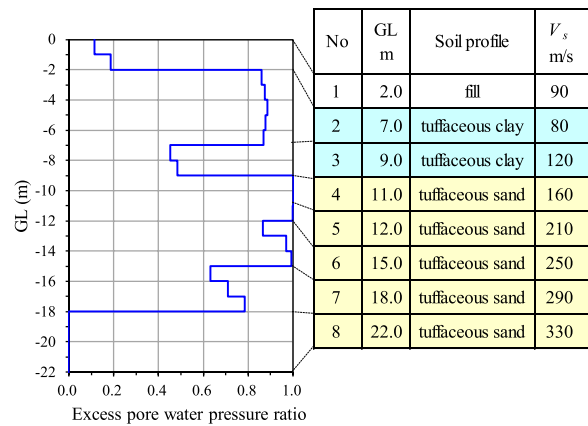
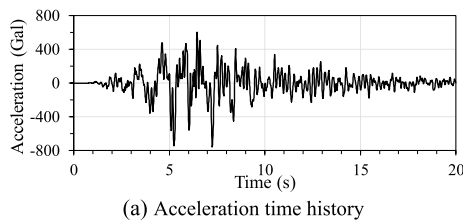
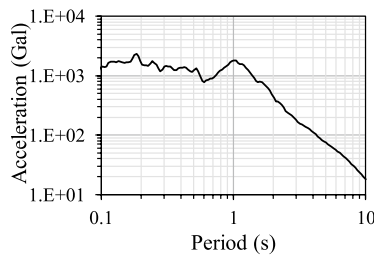


Fig. 26 Maximum distribution of excess pore water pressure ratio at GS-MSK-2

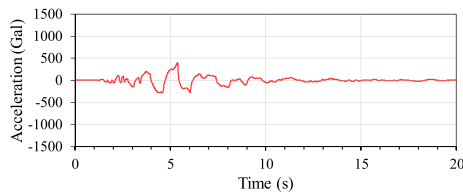


(a) Acceleration time history

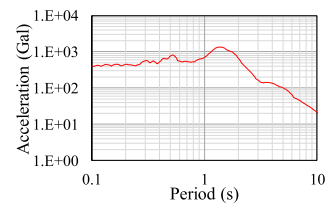


(b) Response spectrum ($h=5\%$)

Fig. 24 Response spectrum of input wave and response spectrum at GS-MSK-2 (GL=75 m, synthesized wave, EW component)

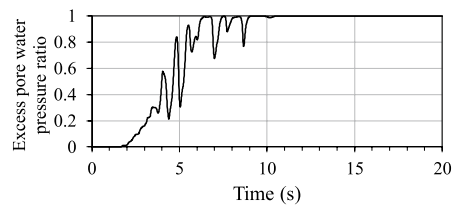


(a) Time history of acceleration

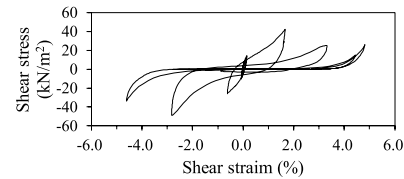


(b) Response spectrum ($h=5\%$)

Fig. 25 Time history of acceleration and response spectrum on the ground surface at GS-MSK-2



(a) Time history of excess pore water pressure ratio



(b) Stress-strain relationship

Fig. 27 Time history of excess pore water pressure ratio and stress-strain relationship in tuffaceous sand layer at GS-MSK-2 (GL=10 m)

considering an elastic substratum condition. It has been estimated from the surface recording motion using the velocity soil profile based on diffuse field theory. The following conclusions were drawn:

- (1) At the KiK-net Mashiki observation station (KMMH16), the observed record of the ground surface was reproduced using the record observed in the borehole.
- (2) Nonlinear time history analysis using the synthesized outcrop wave based on the diffuse field theory also reproduced the recorded wave on the ground surface at KMMH16.
- (3) At the observation point of the MTO, the groundwater level was estimated to be approximately GL-5 m. It was presumed that although the non-linearity of the soil was remarkable, it did not reach liquefaction.

(4) The results of effective stress analysis indicated that liquefaction occurred in the shallow sand layer at the GS-MSK-2 boring site near the Akitsu River. This confirmed that soil liquefaction occurred in areas with thick soft surface layers and a shallower water table along the Akitsu River.


Based on the present study, to reproduce the so-called "heavily damaged belt" that existed between the MTO and GS-MSK-2 sites, modeling of the detailed ground structures and groundwater levels with proper soil properties that do not cause early liquefaction are necessary in that area. Houses around the KMMH16 site did not show high damage ratios, despite the observed high maximum acceleration and velocity. This means that the construction ages of the houses in downtown Mashiki should also be considered because

of the continuous evolution of building codes in Japan. Around the heavily damaged belt, a high percentage of the houses were built before the significant code modifications in 1981 (e.g., Yamada et al. 2017), the average yield capacity of which was estimated to be much less than the houses built after 1982, as seen in the nonlinear structural model constructions in Kobe during the 1995 Hyogo-ken Nanbu earthquake (e.g., Nagato and Kawase 2004; Yoshida et al. 2004). The relationship between the simulated ground motions and observed structural damage ratios in downtown Mashiki was reported in an article by Sun et al. (2021).

Appendix


The parameters of the constitutive equations are shown in Tables 5, 6, 7, 8.

Table 5 Constitutive equation parameters of R–O model at KMMH16 (Kik-net Mashiki)



No.	GL m	Soil profile	R–O model		
			G_{0i} kN/m ²	$\gamma_{0.5i}$	h_{max} %
1	3.0	Volcanic clay	4923	2.197E–4	20
2	9.0	Volcanic clay	12284	1.086E–4	19
3	14.0	Sand	8807	5.123E–5	19
4	15.0	Sand	7910	5.123E–5	19
5	33.0	Pumice tuff (linear)			
6	41.0	Volcanic clay	17284	1.086E–4	19
7	51.0	Sand	62269	5.123E–5	19
8	69.0	Sandy gravel	55348	4.000E–5	22
9	101.0	Tuff breccia (linear)			
10	133.0	Andesite rock (linear)			
11	143.0	Tuff breccia (linear)			
12	167.0	Andesite rock (linear)			
13	200.4	Tuff (linear)			
14	234.0	Andesite rock (linear)			
15	252.0	Andesite rock (linear)			

Table 8 Constitutive equation parameters of R–O and Bowl models at GS-MSK-2



No.	GL m	Soil profile	R–O model			Bowl model					
			G_{0i} kN/m ²	$\gamma_{0.5i}$	h_{max} %	A	C	D	$\frac{C_s}{(1+e_0)}$	$\frac{C_c}{(1+e_0)}$	X_t
1	2.0	Fill	6604			−1.0	8.0	10	0.0500	0.0550	0.11
2	7.0	Tuffaceous clay	2463	1.248E−4	0.23	−1.0	8.0	10	0.0500	0.0550	0.11
3	9.0	Tuffaceous clay	4150	1.248E−4	0.23	−1.0	8.0	10	0.0500	0.0550	0.11
4	11.0	Tuffaceous sand	7107	4.712E−5	0.25	−1.0	8.0	30	0.00600	0.00620	0.11
5	12.0	Tuffaceous sand	11253	4.712E−5	0.25	−1.5	10.0	35	0.00600	0.00615	0.16
6	15.0	Tuffaceous sand	14518	4.712E−5	0.25	−2.0	12.0	40	0.00600	0.00610	0.22
7	18.0	Tuffaceous sand	17424	4.712E−5	0.25	−3.0	15.0	50	0.00600	0.00605	0.30
8	22.0	Tuffaceous sand	20273	4.712E−5	0.25						
9	28.0	Tuffaceous sand	21365	4.712E−5	0.25						
10	35.0	Tuffaceous sand	28204	4.712E−5	0.25						
11	48.0	Tuffaceous gravel	34393	3.500E−5	0.24						
12	53.0	Tuffaceous silty sand	18131	4.712E−5	0.25						
13	60.0	Tuffaceous gravel	27034	3.500E−5	0.24						
14	68.0	Tuffaceous gravel	49629	3.500E−5	0.24						
15	75.0	Tuff (linear)									

Abbreviations

- eIGRA Equivalent-linear ground response analysis
- esGRA Effective-stress ground response analysis
- JMA Japan Meteorological Agency
- nGRA Nonlinear ground response analysis
- NIED National Research Institute for Earth Science and Disaster Resilience in Japan
- NILIM National Institute for Land and Infrastructure Management
- PGA Peak ground acceleration
- NS North–south
- EW East–west
- UD Up–down

Acknowledgements

In this study, earthquake observation records and geophysical structure information obtained and published by NIED (<https://doi.org/10.17598/NIED.0004>) as well as records of a seismic intensity instrument operated by Kumamoto Prefecture and distributed by JMA at https://www.data.jma.go.jp/svd/eqev/data/kyoshin/jishin/1604160125_kumamoto/index2.html were used. We would like to express our deep appreciation to the NIED, Kumamoto Prefecture, and the JMA. We also thank Dr. Masayuki Yoshimi of the National Institute of Advanced Industrial Science and Technology and Dr. Hiroshi Arai of the Building Research Institute for sharing important scientific data for our research. This study was partially supported by the Japan Society for the Promotion of Science (JSPS) Kakenhi Grant-in-Aid for Basic Research (B) Number 19H02405 and donations from Hanshin Consultants Co. Ltd.

Author contributions

Model construction was performed mainly by KF and KY. Theoretical calculations were mainly performed using the KF. Velocity inversion and bedrock motion calculations were conducted by FN with consultation of HK. JS provided the simulation results in the target area for discussion purposes. KF wrote the initial draft of the manuscript in Japanese through a discussion with KY, FN, and HK; KY translated it into English, and HK revised it. The final

manuscript was written and revised by KF, KY, and HK based on discussions among all the authors of this manuscript. All authors have read and approved the final manuscript.

Funding

JSPS Kakenhi Grant-in-Aid for Basic Research (B) Number 19H02405 and the donation from Hanshin Consultants Co, Ltd.

Availability of data and materials

The waveforms used in this study are available from the following organizations: NIED for KMMH16 and JMA for MTO.

Declarations

Competing interests

The authors declare that they have no competing interests.

Consent for publication

Not applicable.

Author details

¹Ohsaki Research Institute, 2-2-2 Uchisaiwai-Cho, Chiyoda-Ku, Tokyo 100-0011, Japan. ²Disaster Prevention Research Institute, Kyoto University, Gokasho, Uji, Kyoto 611-0011, Japan.

Received: 4 July 2022 Accepted: 14 April 2023

Published online: 16 May 2023

References

Aoi S, Obara K, Hori S, Kasahara K, Okada Y (2000) New strong motion observation network KiK-net. Eos Trans AGU 81:329

- Beresnev IA, Wen KL (1996) Nonlinear soil response—a reality? *Bull Seismol Soc Am* 86:1964–1978
- Boulanger RW, Meyers MW, Mejia LH, Idriss IM (1998) Behavior of a fine-grained soil during the Loma Prieta earthquake. *Can Geotech J* 35:146–158
- Elgamal A-W, Zeghal M, Parra E (1996) Liquefaction of reclaimed island in Kobe. *Japan J Geotech Eng* 122(1):39–49
- Finn WDL (1988) Dynamic analysis in geotechnical engineering. In: Von Thun JL (ed) *Earthq Eng Soil Dyn II: Recent Advances in Ground-Motion Evaluation*, ASCE Geotechnical Special Publication 20:523–591
- Finn WDL (1991) Geotechnical engineering aspects of microzonation. *Proc Fourth Int Conf Seismic Zonation Stanford California* 1:199–259
- Finn WDL, Ventura CC, Wu G (1993) Analysis of ground motions at Treasure Island site during 1989 Loma Prieta earthquake. *Soil Dyn Earthq Eng* 12(7):383–390
- Fukutake K (2018) Simulating liquefaction with the three-dimensional effective stress analysis program HIPER (Bowl model) and liquefaction simulation. *Tech Res Report Inst Technol Shimizu Corp* 96:5–18 **(in Japanese with English abstract)**
- Fukutake K, Kiriya T (2018) LEAP-2017 Centrifuge test simulation using HIPER model tests and numerical simulations of liquefaction and lateral spreading. Springer, Berlin, pp 461–479. <https://doi.org/10.1007/978-3-030-22818-7>
- Fukutake K, Jang J (2013) Studies on soil liquefaction and settlement in the Urayasu district using effective stress analyses for the 2011 Off the Pacific Coast of Tohoku earthquake. *J JSCE 1 Special Topic—2011 Great East Japan Earthquake Division A (Invited)*: 307–321
- Fukutake K, Ohtsuki A, Fujikawa S (1992) 3-Dimensional liquefaction analysis for simulating response of ground due to Superstition Hills earthquake 1987. In: *Proc of 27th Annual Convention of JSSMFE* 1103–1106 (in Japanese)
- Fukutake K, Yoshida K, Kawase H and Nagashima F (2020) Simulation analyses of strong ground motion observed at Kik-net Mashiki station during the 2016 Kumamoto Earthquake. In: *Proc 17th World Conf Earthq Eng Sendai Japan*, Paper No. 1d-0093
- Holzer TL, Youd TL (2007) Liquefaction, ground oscillation, and soil deformation at the Wildlife Array. *California Bull Seismol Soc Am* 97(3):961–976. <https://doi.org/10.1785/0120060156>
- Holzer TL, Youd TL, Hanks TC (1989) Dynamics of liquefaction during the 1987 Superstition Hills California earthquake. *Science* 244:56–59
- Holzer TL, Bennett MJ, Ponti DJ, Tinsley JC III (1999) Liquefaction and soil failure during 1994 Northridge earthquake. *J Geotech Geoenviron Eng* 125(6):438–452. [https://doi.org/10.1061/\(ASCE\)1090-0241\(1999\)125:6\(438\)](https://doi.org/10.1061/(ASCE)1090-0241(1999)125:6(438))
- Hushmand B, Scott RF, Crouse CB (1992) In-place calibration of USGS pore pressure transducers at Wildlife Liquefaction Site, California, USA. 1263–1268 In: *Proc. 10th Earthq Eng World Conf, Balkema, Rotterdam, The Netherlands*
- Idriss IM, Boulanger RW (2008) Soil liquefaction during earthquakes. *Earthquake Engineering Research Institute MNO 12*. Oakland CA: Earthq Eng Res Inst
- Idriss IM, Seed HB (1968) Seismic response of horizontal soil layers. *J Soil Mech Found Eng ASCE* 90(SM4):1003–1031
- Iwasaki T (1986) Soil liquefaction studies in Japan: state-of-the-art. *Soil Dyn Earthq Eng* 5(1):2–68. [https://doi.org/10.1016/0267-7261\(86\)90024-2](https://doi.org/10.1016/0267-7261(86)90024-2)
- Kashiwa H, Arai H, Nakagawa H (2019) Soil–structure interaction effects on strong motion records at Mashiki town office during the 2016 Kumamoto Earthquakes. *J Struct Constr Eng AIJ* 84(756):183–193 **(in Japanese with English abstract)**
- Kawase H, Sato T, Fukutake K, Irikura K (1995) Borehole records observed at the port island in Kobe during the Hyogo-ken Nanbu earthquake of 1995 and its simulation. *J Struct Constr Eng AIJ* 475:83–92 **(in Japanese with English abstract)**
- Kawase H, Sanchez-Sesma FJ, Matsushima S (2011) The optimal use of horizontal-to-vertical spectral ratios of earthquake motions for velocity inversions based on diffuse-field theory for plane waves. *Bull Seismol Soc Am* 101(5):2001–2014. <https://doi.org/10.1785/0120100263>
- Kawase H, Matsushima S, Nagashima F, Baoyintu NK (2017) The cause of heavy damage concentration in downtown Mashiki inferred from observed data and field survey. *Earth Planets Space* 69:3. <https://doi.org/10.1186/s40623-016-0591-1>
- Kawase H, Satoh T, Fukutake K (1996) Simulation of the borehole records observed at the Port Island in Kobe, Japan, during the Hyogo-ken Nanbu earthquake of 1995. In: *Proc 11th World Conf Earthq Eng, Acapulco Mexico CD-ROM Ref No. 140* 1–8.
- Kobayashi K, Abe Y, Uetake T, Mashimo M, Kobayashi H (1995) Inversion of spectrum ratio of horizontal to vertical component of preliminary tremors. In: *Proc Architectural Institute of Japan B-1:307–308 (in Japanese)*
- Kurita T, Shingaki Y, Yoshimi M (2020) Fused lasso solutions for physical logging data modeling. *Proc Japan Soc Civil Engineers* 76(4):125–136 **(in Japanese with English abstract)**
- Murono Y (1999) A study on the seismic design method of pile foundations that reflects the non-linear dynamic interaction during strong ground motions. Report of Railway Technical Research Institute **(in Japanese with English abstract)**.
- Nagashima F, Kawase H (2021) The relationship between V_s , V_p , density and depth based on PS-logging data at K-NET and Kik-net sites. *Geophys J Int* 225:1467–1491. <https://doi.org/10.1093/gji/ggab037>
- Nagashima F, Kawase H (2022) Estimation of horizontal amplification factor and incident spectrum at seismic bedrock during strong shaking based on diffuse field concept. *J Japan Assoc Earthq Eng* 22(2):217–236 **(in Japanese with English abstract)**
- Nagashima F, Matsushima S, Kawase H, Sánchez-Sesma FJ, Hayakawa T, Satoh T, Oshima M (2014) Application of horizontal-to-vertical (H/V) spectral ratios of earthquake ground motions to identify subsurface structures at and around the K-NET site in Tohoku. *Japan Bull Seismol Soc Am* 104(5):2288–2302
- Nagashima F, Kawase H, Matsushima S (2017) Estimation of horizontal seismic bedrock motion from vertical surface motion based on horizontal-to-vertical spectral ratios of earthquake motions. In: *Proc 16th World Conf Earthq Eng, Santiago Chile January 9th to 13th 2017 Paper No. 3685*.
- Nagato K, Kawase H (2004) Damage evaluation models of reinforced concrete buildings based on the damage statistics and simulated strong motions during the 1995 Hyogo-ken Nanbu earthquake. *Earthquake Eng Struct Dynam* 33:755–774. <https://doi.org/10.1002/eqe.376>
- Nakagawa H, Kashiwa N, Arai H (2017) Dynamic deformation characteristics and ground motion amplification characteristics of surface ground at the center region of Mashiki town. In: *Proc JAEE Annual Meeting 1–8 (in Japanese with English abstract)*.
- Nakano T, Miyamoto Y, Kawabe H (2018) Nonlinear soil–structure interaction of Mashiki town office subjected to continuous strong motions during The Kumamoto Earthquake. *J Struct Constr Eng AIJ* 83(748):781–791 **(in Japanese with English abstract)**
- National Academies of Sciences Engineering and Medicine (2016) State of the Art and practice in the assessment of earthquake-induced soil liquefaction and its consequences, The National Academies Press Washington DC. <https://doi.org/10.17226/23474>. (<http://www.nap.edu/23474>)
- National Institute for Land and Infrastructure Management (2016) Quick report of the field survey on the building damage by the 2016 Kumamoto Earthquake Technical note of NILIM 929 **(in Japanese)** <http://www.nilim.go.jp/lab/bcg/siryuu/tmn/tmn0929pdf/ks0929.pdf>. Accessed 10 Jun 2022
- National Research Institute for Earth Science and Disaster Resilience (2022a) J-SHIS historical liquefaction map. <http://www.j-shis.bosai.go.jp/labs/liqmap/>. Accessed 12 Mar 2022a
- National Research Institute for Earth Science and Disaster Resilience (2022b) K-NET and Kik-net. <http://www.kyoshin.bosai.go.jp/kyoshin/>. For the 2016 Kumamoto Earthquake see <https://www.kyoshin.bosai.go.jp/cgi-bin/kyoshin/bigeqs/details.cgi?+20160416012500+all+2016/04/16-01:25:00.00%2032.75N%20130.76E%20012km%20M7.3>. Accessed 12 Mar 2022b
- Okada S, Takai N (1999) Classifications of structural types and damage patterns of buildings for earthquake field investigation. *J Struct Constr Eng (Transac AIJ)* 64:65–72. https://doi.org/10.3130/aijs.64.65_5
- Pretell R, Ziotopoulou K, Davis CA (2020) Liquefaction and cyclic softening at Balboa Boulevard during the 1994 Northridge Earthquake. *J Geotech Geoenviron Eng* 147(2). [https://doi.org/10.1061/\(ASCE\)GT.1943-5606.0002417](https://doi.org/10.1061/(ASCE)GT.1943-5606.0002417)
- Prevost JH, Keane CM, Ohbo N, Hayashi, K (1991) Validation of procedures for analysis of liquefaction of sandy soil deposits. In: *5th Int Conf Soil Dyn Earthq Eng* 263–276.
- Schnabel PB, Lysmer J, Seed HB (1972) SHAKE—A computer program for earthquake response analysis of horizontal layered sites. Report No EERC 72-12 University of California Berkeley California USA.

- Shingaki Y, Yoshimi M, Goto H, Kurita T, Sato K, Hosoya T, Arai Y, Morita S (2017) Physical and dynamic properties of the volcanic ash soil in the heavily damaged site of the 2016 Kumamoto Earthquake Mashiki town. *Proc Japan Soc Civil Eng* 73(3):552–559 (in Japanese with English abstract)
- Sun J, Nagashima F, Kawase H, Matsushima S (2020) Site effects analysis of shallow subsurface structures at Mashiki Town, Kumamoto, based on microtremor horizontal-to-vertical spectral ratios. *Bull Seismol Soc Am* 110(6):2912–2938. <https://doi.org/10.1785/0120190318>
- Sun J, Nagashima F, Kawase H, Matsushima S, Baoyintu (2021) Simulation of building damage distribution in downtown Mashiki, Kumamoto, Japan caused by the 2016 Kumamoto Earthquake based on site-specific ground motions and nonlinear structural analyses. *Bull Earthq Eng*. <https://doi.org/10.1007/s10518-021-01119-8>
- Tatsuoka F, Fukushima S (1978) Stress-strain relation of sand for irregular cyclic excitation (1). *Institute of Industrial Science, University of Tokyo* 30(9):26–29 (in Japanese).
- Tatsuoka F, Shibuya S (1992) Deformation characteristics of soils and rocks from field and laboratory tests, Theme Lecture-1. *Proc Ninth Asian Regional Conf Soil Mech Found Eng* 2:101–170
- Wakamatsu K, Senna S, Ozawa K (2017) Liquefaction and its characteristics during the 2016 Kumamoto earthquake. *J Japan Assoc Earthq Eng* 17(4):81–100
- Wotherspoon LM, Orense RP, Jacka M, Green RA, Cox BR, Wood CM (2014) Seismic performance of improved ground sites during the 2010–2011 Canterbury earthquake sequence. *Earthq Spectra* 30(1):111–119
- Yamada M, Ohmura J, Goto H (2017) Wooden building damage analysis in Mashiki town for the 2016 Kumamoto Earthquakes on April 14 and 16. *Earthq Spectra* 33:1555–1572. <https://doi.org/10.1193/090816EQS144M>
- Yamahara H (1970) Ground motions during earthquake and the in-put loss of earthquake to building response (Part 2). *J Struct Constr Eng AIJ* 167:25–30 (in Japanese with English abstract)
- Yoshida K, Hisada Y, Kawase H (2004) Construction of damage prediction model for wooden buildings considering construction age, *Proc of the 2004 Annual Meeting of AIJ, Series B-II 2004* (in Japanese).
- Youd TL (2003) Liquefaction mechanisms and induced ground failure. In: Kanamori H, Jennings PC, Kisslinger C (eds) Lee WHK. *International Handbook on Earthquake and Engineering Seismology*, Academic Press Amsterdam the Netherlands, pp 1159–1174
- Zeghal M, Elgamal A-W (1994) Analysis of site liquefaction using earthquake records. *J Geotech Eng ASCE* 120(6):996–1017

Publisher's Note

Springer Nature remains neutral with regard to jurisdictional claims in published maps and institutional affiliations.

Submit your manuscript to a SpringerOpen[®] journal and benefit from:

- Convenient online submission
- Rigorous peer review
- Open access: articles freely available online
- High visibility within the field
- Retaining the copyright to your article

Submit your next manuscript at ► [springeropen.com](https://www.springeropen.com)
